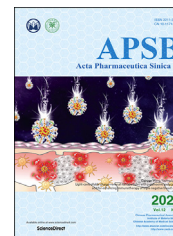




Chinese Pharmaceutical Association  
Institute of Materia Medica, Chinese Academy of Medical Sciences

Acta Pharmaceutica Sinica B

[www.elsevier.com/locate/apsb](http://www.elsevier.com/locate/apsb)  
[www.sciencedirect.com](http://www.sciencedirect.com)



ORIGINAL ARTICLE

# Bioresponsive immune-booster-based prodrug nanogel for cancer immunotherapy



Xianbin Ma<sup>a,†</sup>, Shaochen Yang<sup>b,†</sup>, Tian Zhang<sup>a</sup>, Shuo Wang<sup>b</sup>,  
Qichao Yang<sup>b</sup>, Yao Xiao<sup>b</sup>, Xiaoxiao Shi<sup>c</sup>, Peng Xue<sup>a</sup>, Yuejun Kang<sup>a</sup>,  
Gang Liu<sup>c,\*</sup>, Zhi-Jun Sun<sup>b,\*</sup>, Zhigang Xu<sup>a,\*</sup>

<sup>a</sup>Key Laboratory of Luminescence Analysis and Molecular Sensing (Southwest University), Ministry of Education, School of Materials and Energy & Chongqing Engineering Research Center for Micro-Nano Biomedical Materials and Devices, Southwest University, Chongqing 400715, China

<sup>b</sup>The State Key Laboratory Breeding Base of Basic Science of Stomatology (Hubei-MOST) & Key Laboratory of Oral Biomedicine, Ministry of Education, School and Hospital of Stomatology, Wuhan University, Wuhan 430079, China

<sup>c</sup>State Key Laboratory of Molecular Vaccinology and Molecular Diagnostics & Center for Molecular Imaging and Translational Medicine, School of Public Health, Xiamen University, Xiamen 361102, China

Received 4 February 2021; received in revised form 28 March 2021; accepted 25 April 2021

**Abbreviations:** 5-FU, 5-fluorouracil; 5-ALA, 5-aminolevulinic acid; ALKP, alkaline phosphatase; ALT, alanine aminotransferase; APCs, antigen-presenting cells; AST, aminotransferase; ATP, adenosine triphosphate; AUC, area under curves; Ce6, chlorin e6; CPT-11, irinotecan; CLSM, confocal laser scanning microscope; CRE, creatinine; CRT, calreticulin; DAMPs, damage-associated molecular patterns; DCs, dendritic cells; DDSs, drug delivery systems; DLN, draining lymph nodes; DOX, doxorubicin; DM NGs, doxorubicin-based mannose nanogel; DOC, docetaxel; DTT, D,L-dithiothreitol; FCM, flow cytometry; FDA, Fluorescein diacetate; GEM, gemcitabine; GSH, glutathione; HCPT, 10-hydroxy camptothecin; HCT, hematocrit; H&E, hematoxylin-eosin; HGB, hemoglobin concentration; HMGB1, high migrating group box 1; ICB, immune checkpoint blockade; ICD, immunogenic cell death; ICG, indocyanine Green; IHC, immunohistochemistry; irAEs, immune-related adverse events; ITM, immunosuppressive tumor microenvironment; LDH, lactate dehydrogenase; LYM, lymphocyte ratio; MAN, mannose; MCHC, mean corpuscular hemoglobin concentration; MCSs, multicellular spheroids; MFI, mean fluorescence intensity; MPV, mean platelet volume; NGs, nanogels; OXA, oxaliplatin; P18, purpurin 18; PDI, polydispersity index; PLT, platelets; PTX, paclitaxel; RBC, red blood cell count; RDW, variation coefficient of red blood cell distribution width; TAAs, tumor-associated antigens; TAM, tumor-associated macrophages; TMA, tissue microarrays; TME, tumor microenvironment; TGF- $\beta$ , transforming growth factor- $\beta$ ; Urea, urea nitrogen; WBC, white blood cell count.

\*Corresponding authors. Tel./fax: +86 23 68253792 (Zhigang Xu); +86 27 87686108 (Zhi-Jun Sun); +86 592 2880648 (Gang Liu).

E-mail addresses: [gangliu.cmitm@xmu.edu.cn](mailto:gangliu.cmitm@xmu.edu.cn) (Gang Liu), [sunzj@whu.edu.cn](mailto:sunzj@whu.edu.cn) (Zhi-Jun Sun), [zgxu@swu.edu.cn](mailto:zgxu@swu.edu.cn) (Zhigang Xu).

<sup>†</sup>These authors made equal contributions to this work.

Peer review under responsibility of Chinese Pharmaceutical Association and Institute of Materia Medica, Chinese Academy of Medical Sciences.

<https://doi.org/10.1016/j.apsb.2021.05.016>

2211-3835 © 2022 Chinese Pharmaceutical Association and Institute of Materia Medica, Chinese Academy of Medical Sciences. Production and hosting by Elsevier B.V. This is an open access article under the CC BY-NC-ND license (<http://creativecommons.org/licenses/by-nc-nd/4.0/>).

## KEY WORDS

Bioresponsive;  
Prodrug;  
Nanogel;  
Doxorubicin;  
Mannose;  
Immunogenic cell death;  
Chemotherapy;  
Immunotherapy

**Abstract** The combination of chemotherapy and immunotherapy motivates a potent immune system by triggering immunogenic cell death (ICD), showing great potential in inhibiting tumor growth and improving the immunosuppressive tumor microenvironment (ITM). However, the therapeutic effectiveness has been restricted by inferior drug bioavailability. Herein, we reported a universal bioresponsive doxorubicin (DOX)-based nanogel to achieve tumor-specific co-delivery of drugs. DOX-based mannose nanogels (DM NGs) was designed and choosed as an example to elucidate the mechanism of combined chemo-immunotherapy. As expected, the DM NGs exhibited prominent micellar stability, selective drug release and prolonged survival time, benefited from the enhanced tumor permeability and prolonged blood circulation. We discovered that the DOX delivered by DM NGs could induce powerful anti-tumor immune response facilitated by promoting ICD. Meanwhile, the released mannose from DM NGs was proved as a powerful and synergetic treatment for breast cancer *in vitro* and *in vivo*, via damaging the glucose metabolism in glycolysis and the tricarboxylic acid cycle. Overall, the regulation of tumor microenvironment with DOX-based nanogel is expected to be an effectual candidate strategy to overcome the current limitations of ICD-based immunotherapy, offering a paradigm for the exploitation of immunomodulatory nanomedicines.

© 2022 Chinese Pharmaceutical Association and Institute of Materia Medica, Chinese Academy of Medical Sciences. Production and hosting by Elsevier B.V. This is an open access article under the CC BY-NC-ND license (<http://creativecommons.org/licenses/by-nc-nd/4.0/>).

## 1. Introduction

Immune checkpoint blockade (ICB)-based immunotherapy has emerged to revolutionize the traditional tumor treatment and subvert the clinical research pattern, showing promising potential in overcoming chemoresistance and improving the survival rate of cancer patients<sup>1–4</sup>. However, the unfavorable patient response rate, immune-related adverse events and expensive cost impeded the development of ICB therapy<sup>5–8</sup>. Recent evidence suggested that cell death caused by certain treatment can induce tumor cells to generate specific tumor immunity<sup>9–11</sup>. Such an immunogenic cell death (ICD), characterized by releasing damage-associated molecular patterns (DAMPs) from dying tumor cells, was conducive to promote antigen presentation and T-cell infiltration<sup>12–15</sup>. To be precise, the antigen-presenting cells (APCs) were inclined to mature once the arrival of dying cells-produced DAMPs, thus activating the effector T-cell to respond against tumor-specific antigens<sup>16,17</sup>. Then, the activated effector T cells were rapidly transported into the tumor, and then infiltrated the tumor site, recognized and killed cancer cells<sup>18</sup>. In short, ICD can promote the stimulation of immune cells against tumor, which can be applied for tumor therapy.

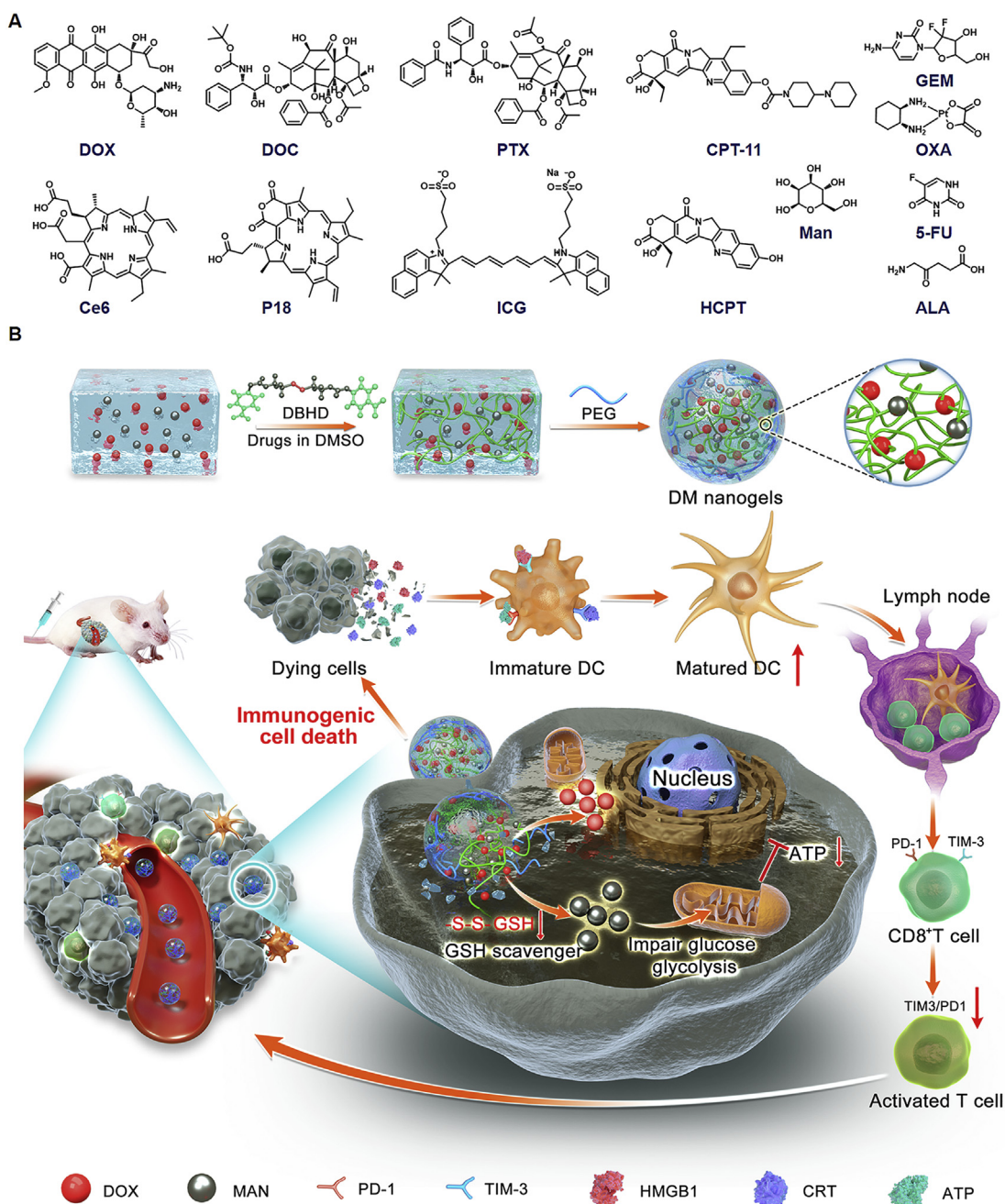
Studies have demonstrated that ICD can be induced by doxorubicin (DOX) for its certain immunomodulatory effects, thus promoting the maturation of immune cells and ameliorating the immune microenvironment<sup>19–21</sup>. Ulteriorly, ICD is characterized by translocation and clustering of calreticulin (CRT) from tumor cells to the cell membrane, which was recognized and phagocytosed by dendritic cells (DCs), thus activating the anti-tumor immune response<sup>22–24</sup>. High mobility group box 1 protein (HMGB1) in tumor cells also play a pivotal role in stimulating antigen-presenting DCs, and secreting adenosine triphosphate (ATP) to recruit DCs into tumor bed<sup>25,26</sup>. Therefore, the induction of ICD is an effective immunogenic therapy to prevent the aggressiveness and metastasis of cancer.

Nanotechnology-based drug delivery systems (DDSs) exhibited favorable tumor accumulation and deep tumor penetration<sup>27–30</sup>, which performed superior therapeutic efficacy in comparison with conventional medicines<sup>31–33</sup>. Nanogels (NGs) formed by intramolecular

cross-linking can integrate good biocompatibility, environmental responsiveness, high stability and low toxicity into one single platform, holding a great promise in designing tailored DDSs<sup>34–37</sup>. As we know, tumor microenvironment (TME) shows various specific features such as highly up-regulated reductive glutathione (GSH) or acidic microenvironment<sup>38–41</sup>. Therefore, it is an optimal choice to develop TME-responsive NGs as DDSs for the treatment of malignancy<sup>42–46</sup>.

Glucose metabolism through glycolysis in cancer cells was significantly faster than normal cells on account of Warburg effect<sup>47–50</sup>. The glycolysis of cancer cells can be suppressed by glucose metabolism inhibitor (such as 2-DG), leading to cancer cell apoptosis<sup>51</sup>. Mannose is the only glyconutrient currently utilized in clinic, which can be directly used to form glycoproteins and participate in immune regulation. Zhang et al.<sup>52</sup> reported that mannose could activate transforming growth factor- $\beta$  (TGF- $\beta$ ) signaling, thereby enhancing the production of Treg cells in T cells. Mannose was engulfed by cells through the same transporter as glucose, which may affect glucose uptake of tumor cells<sup>53</sup>. Recently, Gonzalez et al.<sup>54</sup> have confirmed that oral co-administration of mannose and chemotherapeutic drug can effectively facilitate tumor cell apoptosis *in vitro* and delay the growth of tumor models *in vivo*, while mannose-loaded nanoparticles may accelerate cellular uptake and immune system regulation<sup>55</sup>. Therefore, we hypothesized that the delivery of a large amount of mannose to the tumor site would be good adjuvant therapy for chemotherapy, which may significantly inhibit tumor growth, simultaneously improve the restriction on the immunosuppressive tumor microenvironment (ITM).

Herein, we reported a universal and versatile strategy for engineering DOX-based NGs by conjugating hydroxyl-containing DOX with hydroxyl-containing drugs *via* GSH-sensitive-SS- bond as linker (Scheme 1). The formed NGs could release the loaded drugs after being internalized into TME with high GSH concentration for realizing combination chemo-immunotherapy. The feasibility of cross-linking method has been proved in our previous work<sup>39</sup>. For further proof-of-idea, DOX-based mannose NGs (donated as DM NGs) have been developed. Concretely, DOX could perform chemotherapy to induce ICD of the tumor cells, manifested by the released HMGB1 and exposed CRT to the cell



**Scheme 1** Schematic illustration of bioresponsive doxorubicin-based mannose nanobackpack for cancer immunotherapy by enhancing ICD induction. (A) Drugs that we tested for making DOX-based nanogels with high drug loading including docetaxel (DOC), paclitaxel (PTX), irinotecan (CPT-11), gemcitabine (GEM), oxaliplatin (OXA), chlorin e6 (Ce6), purpurin 18 (P18), indocyanine Green (ICG), 10-hydroxy camptothecin (HCPT), 5-fluorouracil (5-FU), 5-aminolevulinic acid (5-ALA) and mannose. (B) The synthesis process of DOX-based nanogel and simplified mechanism mediated chemo-immunotherapy to inhibit tumor growth by up-regulation immunogenic cell death.

membrane surface to cause an anti-tumor immune response. *In vitro* and *in vivo* experiments confirmed the superiority of DM NGs over other formulation at an equivalent DOX concentration. In addition, the effects of DM NGs on TME modulation were evaluated, including maturation of DCs and relief of exhausted TIM3<sup>+</sup>PD-1<sup>+</sup> T cells. This GSH-responsive DM NGs could systematically regulate the TME and maximize the immune-regulation effects of mannose, indicating the promising application prospects in chemo-immunotherapy against solid tumors.

## 2. Materials and methods

### 2.1. Synthesis of DM NGs

The DOX-based NGs was prepared by one-step cross-linking of DBHD. Typically, 6  $\mu\text{mol}$  of DOX and 11  $\mu\text{mol}$  of mannose were dissolved in 1.5 mL of the DMSO, 3  $\mu\text{mol}$  of DBHD dissolved in 0.15 mL of anhydrous DMSO and added to the reaction solution under stirring. After that, 10  $\mu\text{L}$  of TEA was added in above

solution and reacted at 55 °C for 12 h in the dark. Next, 2  $\mu\text{mol}$  of PEG-NH<sub>2</sub> dissolved in 1.5 mL of DMSO was added into solution under stirring, and the reaction was continued for 12 h in dark. Finally, the reacted DMSO solution was dialyzed against double-distilled water in dialysis bag (MWCO = 3500) to obtain an amphiphilic prodrug NGs. The DOX NGs and mannose NGs (MAN NGs) were also prepared by above method. The drug loading efficiency and encapsulation efficiency were calculated as shown in Eqs. (1) and (2):

$$\text{Loading efficiency (\%)} = \frac{\text{Weight of loaded DOX}}{\text{Weight of NGs}} \times 100 \quad (1)$$

$$\text{Encapsulation efficiency (\%)} = \frac{\text{Weight of DOX}}{\text{Weight of NGs in feeding}} \times 100 \quad (2)$$

## 2.2. Colloidal stability

To better study the stability of the NGs during treatment, the particle size and zeta potential of DM NGs were measured by dynamic light scattering (DLS, Nano ZS90 Malvern) after dispersing for 15 days. Otherwise, the size and polydispersity index (PDI) in different media [PBS or Dulbecco's modified Eagle medium (DMEM) containing 10% FBS] were also monitored.

## 2.3. Drug release *in vitro*

High up-regulated GSH was a significant feature of tumor tissue. To stimulate the redox conditions of tumor tissue, the DOX release from DM NGs was evaluated under different GSH concentrations *in vitro*. D,L-Dithiothreitol (DTT) was often used to simulate the reduction status at the tumor site. Firstly, the DM NGs with the concentration of 200  $\mu\text{g}/\text{mL}$  were added into the dialysis bags (MWCO = 3500) and co-incubated under physiological (pH = 7.4) and redox conditions (10 mmol/L DTT solution) for 72 h. At predetermined time points, the sample was collected and replaced with different concentrations of DTT solution. Finally, the concentration of DOX in collected samples were quantified with a fluorescence microplate reader (Tecan, SPARK-10M).

## 2.4. Cell culture

4T1 mouse breast cancer cells were cultured in DMEM supplemented with 10% FBS and 1% Pen/Strep. The cells were cultured at 37 °C under 5% CO<sub>2</sub> atmosphere and subcultured after the cells in the culture flask were almost confluent.

## 2.5. *In vitro* cytotoxicity study

The cytotoxicity test was quantified according to the standard 3-(4,5)-dimethylthiazolium (-z-y1)-3,5-di-phenyltetrazoliumromide (MTT) approach. Firstly, 4T1 cells were seeded in 96-well plate with a density of  $1 \times 10^4$  per well. After cell adherence, the old DMEM was removed and replaced with fresh DMEM medium containing free DOX, free mannose, MAN NGs, DOX NGs and DM NGs, the group without treatment was used as control. Then all the cells were incubated for 24 h. Thereafter, the DMEM containing drugs were replaced with 100  $\mu\text{L}$  of MTT solution and incubated for another 4 h. Then the MTT solutions was removed

gently and replaced with 100  $\mu\text{L}$  of DMSO. Finally, the absorbance at 590 nm was recorded by a microplate reader.

## 2.6. Live cell staining

To verify the cytotoxicity of different treatments, 4T1 cells were seeded in 12-well plate ( $1.3 \times 10^5$  cells per well) and then incubated with different drugs (free DOX, free mannose, MAN NGs, DOX NGs and DM NGs). After incubating for 24 h (DOX concentration: 10  $\mu\text{g}/\text{mL}$ ), the old DMEM medium was removed and the cells were washed with PBS twice. Finally, the live cells were visualized after co-staining with fluorescein diacetate (FDA) for 30 min and observed with a fluorescence microscope (Olympus, IX 73). The area occupied by live cells were measured by Image-J software (NIH, USA).

## 2.7. Wound healing assay

4T1 cells were cultured in 6-well plate until confluence. The wound was made by sterilized 200  $\mu\text{L}$  pipet tips, and then washed with PBS twice to remove the displaced cells. The cells were incubated with different drugs (free DOX, free mannose, MAN NGs, DOX NGs and DM NGs) for 24 h (DOX concentration: 10  $\mu\text{g}/\text{mL}$ ), and the images were obtained at 0 and 24 h.

## 2.8. Cellular uptake study

To evaluate the cellular uptake of DM NGs, the 4T1 cells were seeded into 8-well plate with a density of  $3 \times 10^4$  cells per well, and incubated with DMEM overnight. Next, the cell was washed with PBS twice and incubated with fresh medium containing DM NGs for 4 h. Then the lysosomes was stained with Lyso-Tracker Green dye for 45 min and then Hoechst33342 for 15 min. Lastly, the photograph was collected by confocal laser scanning microscope (CLSM, Zeiss 800). The CLSM was also used to observe the distribution of DM NGs in 4T1 cell, 4T1 cells were seeded into 12-well plate and cultured overnight. After the adherence of cells, old medium was replaced with fresh medium containing DM NGs (DOX concentration: 20  $\mu\text{g}/\text{mL}$ ). After the cells were cultured with DM NGs for 1 and 2 h, old medium was discarded and the cells were washed with PBS, fixed with paraformaldehyde for 20 min and then stained with AF-488 for 45 min. Furthermore, the nucleus was stained with DAPI for 5 min. Finally, the fluorescence was observed by CLSM. Furthermore, the fluorescence intensity of DOX in the cells was also obtained by flow cytometry (FCM, NovoCyte 2060R, USA). The cells were cultured as above description. The cells were treated with free DOX, DOX NGs and DM NGs (DOX concentration = 10  $\mu\text{g}/\text{mL}$ ) for 10, 30 min, 1 and 2 h, respectively. And the cells without treatment were set as control. After that, the 4T1 cells were digested, the phagocytic rate of the cells was measured by FCM, and the intracellular fluorescence intensity was also quantified.

## 2.9. The GSH consumption *in vitro*

GSH was an active tripeptide naturally occurring in cells, which played roles in antioxidant regulation, immune regulation and redox signal regulation. GSH was rich in cancer cells and the altered GSH level would make significant effects on chemotherapy. The ThiolTracker Violet was used to measure the consumption of GSH *in vitro*. The DM NGs (DOX concentration:

20  $\mu\text{g}/\text{mL}$ ) cover the 4T1 cells (with the density of  $3 \times 10^4$  cells per well) for 4 h. Afterward, the picture was obtained by CLSM.

### 2.10. Intracellular ATP evaluation

The 4T1 cells were seeded into 6-well plate ( $1 \times 10^5$  cells per well) overnight. After treating with various drugs for another 36 h, all the groups were incubated with ATP Assay Kit according to the manufacturer's recommended protocols. The group without the treatment was set as control.

### 2.11. In vitro penetration

Multicellular spheroids (MCSs) were obtained according to our previous report<sup>39</sup>. Briefly, the cell suspension was seed into the 96-well plate ( $1 \times 10^3$  cells per well), and 50  $\mu\text{L}$  of 1% TAE working solution was added in the plate wells. After incubating for about 5 days, the MCSs were treated with DM NGs (DOX concentration = 20  $\mu\text{g}/\text{mL}$ ) for 4, 8 and 24 h, respectively. Finally, the image was taken by CLSM.

### 2.12. ICD induced by DM NGs in vitro

The intracellular HMGB1 distribution and CRT expression on the surface of tumor cells were evaluated by immunofluorescence analysis. Briefly, 4T1 cells were seeded in 12-well plates ( $3 \times 10^4$  cells per well). After cell adherence, the cells were treated with the various drugs at an equivalent DOX concentration (10  $\mu\text{g}/\text{mL}$ ) for 24 h. The cells were then washed with PBS twice, and fixed with 4% paraformaldehyde for 20 min and permeabilized with 0.1% Triton X-100 for 20 min. Next, the cells were blocked with 5% BSA, and then incubated with primary antibody overnight. Lastly, the primary antibody was replaced by the fluorescence labeled-secondary antibody for 30 min. The cells were then stained with DAPI for 10 min and examined by CLSM.

### 2.13. Animals and tumor models

All animal experiments were carried out and approved by the University Committee on Use and Care of Animals (UCUCA) at Southwest University. 5–6 week-old female BALB/c mice (18–20 g, for evaluating biodistribution and therapeutic efficacy), 7–8 week-old female Kunming mice (30–35 g, for routine blood test) and SD rats (180–220 g, for pharmacokinetic study) were supplied by Chengdu Dashuo Experimental Animal Co., Ltd. (Chengdu, China). The tumors of mice were established by subcutaneous injection of  $1 \times 10^6$  4T1 cells.

### 2.14. Pharmacokinetic and biodistribution studies

For pharmacokinetic study, the SD mice (180–220 g) were randomly divided into two groups ( $n = 3$ ) and intravenously administered with free DOX and DM NGs at a dose of 5 mg/kg *via* tail vein. At predetermined time points (0.33, 0.5, 1, 3, 5, 7, 9, 12 and 24 h), the blood was collected from the eyelid of the mice. Firstly, the collected blood samples were centrifuged at  $664 \times g$  for 10 min by Centrifuge (Sigma, Germany) to obtain plasma. 50  $\mu\text{L}$  of plasma was taken, and 150  $\mu\text{L}$  of diethyl ether was added for protein sedimentation. Subsequently, the mixed solution was centrifuged for 10 min. Lastly, the concentration of DOX in plasma was measured by fluorescence microplate reader.

To evaluate the biodistribution of DM NGs in the mice, a fluorescence probe DIR was introduced into DM NGs by adding

the DIR to the nanogel. The DM-DIR NGs were synthesized with the same method as DM NGs. The concentration of DIR was quantified by a UV spectrum according to the standard curve line. Then mice bearing tumor were randomly divided into 2 groups ( $n = 3$ ). And the mice were intravenously injected with DM-DIR NGs and free DIR, respectively, *via* the tail vein at a DIR dose of 2.0 mg/kg. The photographs were obtained by using imaging system (FX Pro, USA) at 6, 12, 24, 48 and 72 h. After 72 h, the mice were sacrificed, the main organs and tumor tissues were also analyzed using FX Pro to see the *ex vivo* fluorescence distribution. The fluorescence of mice and organs were measured by Image-J software.

The concentration of DOX in major organs and tumor tissues were also measured. After injection for 72 h, the major organs and tumor were collected, washed with saline and then homogenized in 1 mL PBS containing 0.1 M NaOH and SDS. After that, 1 mL of chloroform-methanol (4:1, *v/v*) was added to extract DOX. Finally, the DOX concentration in tissue was measured by FT-IR spectrophotometer after centrifuging to collect the organic phase.

### 2.15. In vivo antitumor efficiency and biosafety

4T1-tumor-bearing mice were divided into six groups ( $n = 5$  per group) and received further intravenous administration: Groups 1: control group (only intravenous injection with saline); Groups 2: free DOX; Groups 3: free MAN; Groups 4: MAN NGs; Groups 5: DOX NGs; Groups 6: DM NGs. The mannose dose in groups 3, 4, 6 was equivalent and set as 3.0 mg/kg. And the DOX dose in groups 2, 5, 6 was equivalent and set as 5.0 mg/kg. The experiment began after the tumor volume reached approximately 100  $\text{mm}^3$ . The tumor volume and body weight of mice were recorded every other day, and the volumes were determined as shown in Eq. (3):

$$\text{Volume} = 0.5 \times (\text{Length}) \times (\text{Width})^2 \quad (3)$$

After 11 days of various treatments, the mice were sacrificed and the tumor tissue sections and major organs were taken for Hematoxylin–Eosin (H&E) staining. Meanwhile, the tumor tissue section was further analyzed with TNUEL and Ki67 staining. In addition, blood samples were collected to analyze the serum levels of the alanine aminotransferase (ALT), aminotransferase (AST), creatinine (CRE), urea nitrogen (urea), lactate dehydrogenase (LDH) and alkaline phosphatase (ALKP). The saline group was set as control.

### 2.16. Immunohistochemistry (IHC) and immunofluorescence analysis

Tissue microarray slides of each groups were used for IHC. The 4- $\mu\text{m}$  slides were put in 62 °C oven for 2 h, then deparaffinized, dehydrated, followed by antigen retrieval citrate buffer (pH = 6.0) at high pressure and high temperature. After that, we quenched the slides in 3% hydrogen superoxide at 37 °C. Nonspecific binding was prevented by blocking with 10% goat serum at 37 °C for 20 min. Slides for IHC staining were incubated with anti-CD8 (cell signaling technology) and anti-granzym B (cell signaling technology) overnight at 4 °C. Before staining, slides were incubated with secondary antibody and avidin-biotin-peroxidase at 37 °C for 1 h. After incubating with 3,3'-diaminobenzidine tetrachloride, slides were counterstained using Mayer's hematoxylin. All treated slides were subsequently covered by coverslips. For immunofluorescence staining, slides were incubated in 10%

goat serum at 37 °C for 1 h, primary antibodies: anti-HMGB1 antibody or anti-CRT were applied to incubate overnight at 4 °C freezer. The next day, slides were incubated with secondary antibody for 1 h and stained with DAPI for 5 min (Alexa 594 anti-rabbit Invitrogen and Alexa 488 Yeasen 34506ES60). All the IHC slices were scanned with Panoramic DESK digital pathology scanner (3D HISTECH). And all the immunofluorescence staining slices were scanned with CLSM.

### 2.17. Flow cytometry analysis

Tumors and draining lymph nodes (DLN) of 4T1 mouse model were collected and processed to single-cell suspension for flow cytometric analysis. The cells were analyzed by FlowJo (Treestar, Ashland, OR, USA).

### 2.18. Hemolysis assay

The fresh blood was taken from the mice eyelids in EDTA-anticoagulant tube. Then the fresh blood was centrifuged at 664×g for 15 min to collect red blood cells (RBC). The obtained RBC was washed and diluted with PBS (pH = 7.4). Then 0.3 mL of RBC and 0.3 mL of different concentrations of DM NGs (equivalent to 500, 200, 100, 50, 10, 5 and 1 µg/mL of DOX) were cultured for 2 h. Furthermore, the 1% of Triton X-100 and PBS (pH = 7.4) were served as positive and negative controls, respectively. Finally, the samples were centrifuged and the absorbance was measured by UV–Vis. The hemolysis rate was calculated as shown in Eq. (4):

$$\text{Hemolysis (\%)} = (A_{\text{sample}} - A_{\text{negative}}) / (A_{\text{positive}} - A_{\text{negative}}) \times 100 \quad (4)$$

### 2.19. In vivo toxicity evaluation

In order to study the side effects of different treatments on healthy mice, the Kunming mice were randomly divided into 6 groups ( $n = 4$ ) and injected with different drugs through the tail vein according to their weight (5 mg/kg). The body weight of mice was recorded every day. Seven days later, blood was collected for routine blood test and the major organs were collected for H&E staining. The routine blood test was performed with Mindray BC-2600 Vet hematology analyzer, in which the parameters included white blood cell count (WBC), hematocrit (HCT), lymphocyte ratio (LYM), red blood cell count (RBC), hemoglobin concentration (HGB), variation coefficient of red blood cell distribution width (RDW), mean corpuscular hemoglobin concentration (MCHC), mean platelet volume (MPV) and platelets (PLT).

## 3. Results

### 3.1. Preparation and characterization of DM NGs

To prepare prodrug NGs according to our design, a bioresponsive crosslinking agent with disulfide bond and two nitrophenyl groups was synthesized (denoted as DBHD), which could link small drug molecules by hydroxy or amino groups, resulting in nano-sized hydrogel. The successful synthesis of DBHD was confirmed by  $^1\text{H}$  NMR and  $^{13}\text{C}$  NMR spectra (Supporting Information Fig. S1–S3). To obtain the expected prodrug NGs, a series of optimizing indexes including molar ratio of drugs, solvents, pH value and temperatures were detailed assessed (Supporting Information

Figs. S4–S5, Table S1). Finally, the prodrug NGs were prepared in DMSO at 55 °C. The obtained prodrug NGs could be decomposed under reductive TME, thus releasing drug molecules for therapeutic applications. To demonstrate the universality of DOX-based NGs, a library of chemotherapeutics (*e.g.*, docetaxel, paclitaxel, irinotecan, gemcitabine, oxaliplatin, 10-hydroxy camptothecin, 5-fluorouracil), photosensitizer (*e.g.*, chlorin e6, purpurin 18, indocyanine Green, 5-aminolevulinic acid), and immune regulator (*e.g.*, mannose) were screened. All the drugs that we tested could form stable nanogel with DOX, with high drug loading capacity. Such nanogel can be a promising platform for the encapsulation of diverse anti-cancer drugs (Supporting Information Fig. S6).

To fabricate DM NGs, DOX and MAN molecules were introduced into the DM NGs through the DBHD (Scheme 1). The DOX NGs and MAN NGs were also synthesized with the same method. The encapsulation efficiency and loading efficiency of DOX in the DM NGs were  $88.7 \pm 3.2\%$  and  $58.7 \pm 4.5\%$ , respectively. The hydrodynamic diameter and zeta potential of DM NGs were  $86.08 \pm 2.87$  nm (PDI =  $0.25 \pm 0.04$ ) and  $-8.35 \pm 0.57$  mV, respectively. Kindly, the medium such as PBS (pH = 7.4) and DMEM did not affect the hydrodynamic diameter of DM NGs (Supporting Information Fig. S7), which was beneficial to prolong the retention time *in vivo*. The morphology of DM NGs was observed to be spherical by TEM (JEM-1230EX) (Fig. 1A). Spherical morphology and near-neutral surface charges would facilitate the circulation of DM NGs in the blood. The zeta potential of MAN NGs and DOX NGs were also measured (Fig. 1C). The DM NGs showed no obvious size and potential change during the storage of 15 days, demonstrating that DM NGs had good biological compatibility and stability (Fig. 1B). The presence of DOX and MAN were confirmed by UV–Vis (Shimadzu Corporation, Japan), fluorescence spectra (Thermo Nicolet 6700 FT-IR, USA) and mass spectra (Bruker, Germany), respectively (Fig. 1D and Supporting Information Fig. S8). The disulfide bond in DM NGs would be broken upon the activation of high GSH level in TME, thus drugs could be released from the DM NGs (Fig. 1E). As depicted in Fig. 1F, nearly 20% of DOX was released in PBS at 72 h. In contrast, about 75% of DOX were released in 10 mmol/L DTT solution. Such selective release model towards reductive TME would slow down the side-effects of chemotherapy and burst forth.

### 3.2. Cellular uptake and cytotoxicity in vitro

Time-dependent cellular uptake of DM NGs was demonstrated by FCM analysis and CLSM. After the DM NGs entered into the cells, the disulfide bond can be activated with the overexpressed GSH in tumor cells thus releasing drugs. Compared with free DOX group, the DM NGs can be effectively engulfed by tumor cell, and a maximal phagocytosis could be obtained within 2 h (Fig. 1G and Supporting Information Figs. S9 and S10). Afterwards, the CLSM was employed to evaluate the cell uptake and drug distribution. Cellular colocalization experiment revealed that the DM NGs successfully entered into lysosome. The location of red fluorescence of the DOX was close to that of blue lysosomal dye, with a high Mander's coefficients of 0.84, indicating that the DM NGs could be easily internalized by 4T1 cells (Fig. 1H and Supporting Information Fig. S11). As shown in Fig. 1I and Supporting Information Fig. S12, the fluorescence of intracellular DOX gradually became stronger, suggesting that the DM NGs could be effectively uptaken and accumulated in 4T1 cells.

Next, it is essential to detect the intracellular GSH depletion by the abundant disulfide bond of DM NGs. Thiol-Tracker Violet was applied as a fluorescence probe to explore the consumption process. As shown in Fig. 1J and K, bright green fluorescence was observed in the control group, while the green fluorescence was obviously decreased after the treatment of DM NGs in 4T1 cells, demonstrating the effective consumption of GSH<sup>56,57</sup>. The depleting of GSH led to the disintegration of DM NGs structure and the release of loaded drugs, thus inducing cell death. All above results suggested that the DM NGs would be a promising system for cancer therapy.

Then the cytotoxicity of the DM NGs was evaluated. As shown in Fig. 2A, the viability of 4T1 cells was highly dependent on the dosage of drugs. The free DOX showed strong toxicity to 4T1 cells, even at a low concentration of 0.1  $\mu\text{g}/\text{mL}$ . Only about 70% of the cells survived, while free mannose and MAN NGs were almost non-toxic to cells at low concentrations. After the concentration of mannose reached 20  $\mu\text{g}/\text{mL}$ , the cell viability of free mannose and MAN NGs were about 85% and 75%, respectively. At an equivalent concentration of DOX, the cytotoxic effects of DM NGs were greater than that of DOX NGs, indicating that the

mannose may make certain killing effects on 4T1 cells. It might be due to that mannose can affect 4T1 cell apoptosis through the endogenous pathways of BAX and BAK (essential factors for mitochondria membrane permeabilization), thus making 4T1 cells more sensitive to DOX<sup>54</sup>. Another reason may be that DM NGs exhibited faster cell phagocytosis than DOX NGs, consistent with previous FCM results (Supporting Information Fig. S10).

*In vitro* cytotoxicity was further evaluated on 4T1 cells by cell counting. After adding different drugs, the number of cells was recorded for 24 h. As indicated (Supporting Information Fig. S13), the variation tendency of number of cells treated with different drugs was similar to that of the MTT assay. Free mannose and MAN NGs also delayed the growth of 4T1 cells. At each concentration, the treatment of free DOX, DOX NGs and DM NGs efficiently inhibited 4T1 cell proliferation and reduced cell viability, indicating the high anti-cancer activity of above three drugs. The cytotoxicity of various drugs were further examined by fluorescence imaging of live cells using FDA, in which the live cells were visualized as green fluorescence (Fig. 2B and C). When the cells were incubated with free mannose and MAN NGs, the cells grew in looser state than that of control group. The mannose

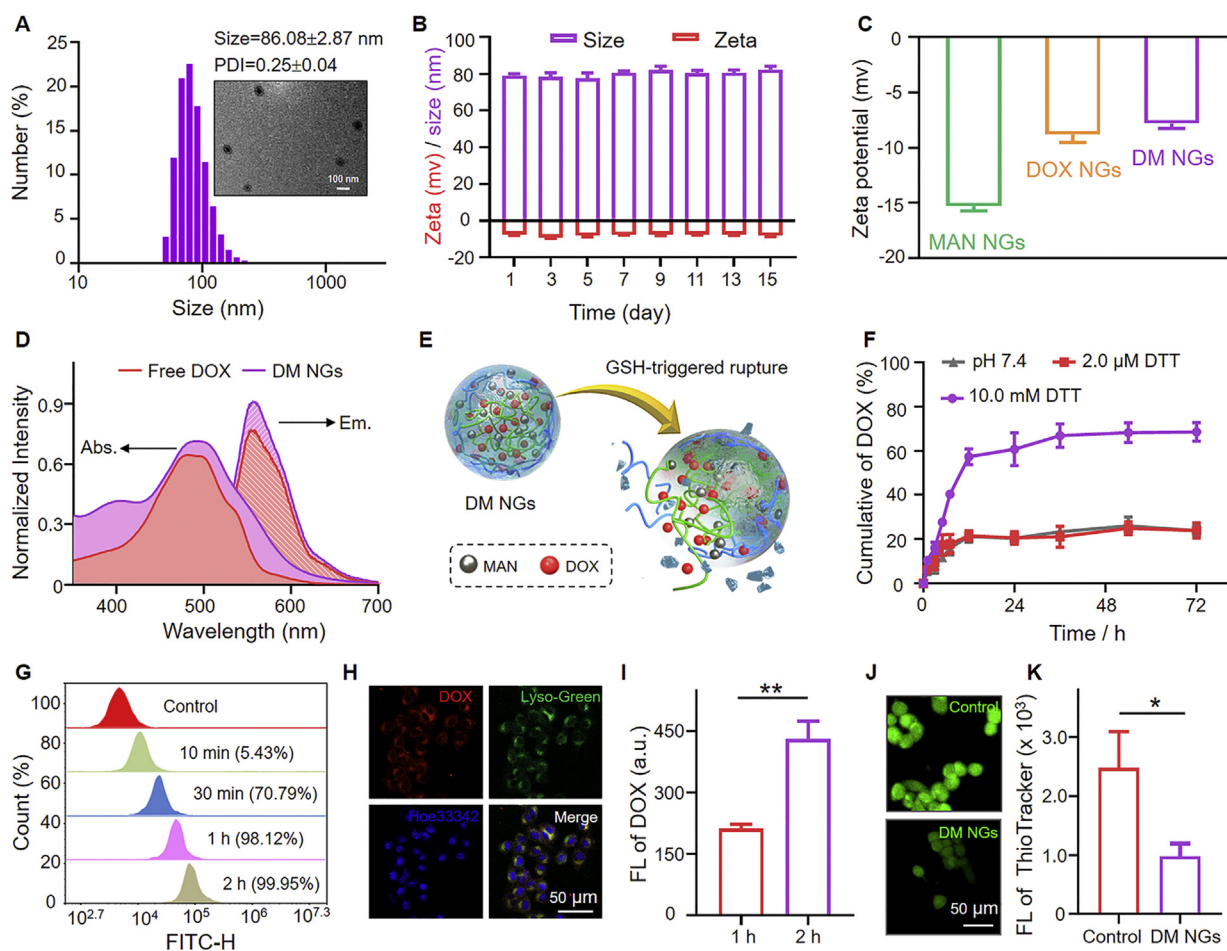


**Figure 1** Characterization of DM NGs. (A) Hydrodynamic diameter ( $D_h$ ) and TEM image of DM NGs. (B) The change in hydrodynamic diameter and zeta potential of DM NGs in 15 days. (C) Zeta potentials of MAN NGs, DOX NGs and DM NGs. (D) UV-Vis spectra and fluorescence spectra of Free DOX and DM NGs. (E) The controlled release behavior of DM NGs after GSH treatment. (F) *In vitro* release pattern of DOX from DM NGs. (G) Flow cytometric profile of DM NGs. (H) CLSM images of lysosomal colocalization. (I) Quantification of intracellular DOX in 4T1 cells for 1 and 2 h. (J) GSH level was stained by Thiol-Tracker Violet (green). (K) The quantification of intracellular GSH in 4T1 cells. Data are presented as mean  $\pm$  SD ( $n = 3$ ). \* $P < 0.05$ ; \*\* $P < 0.01$ .

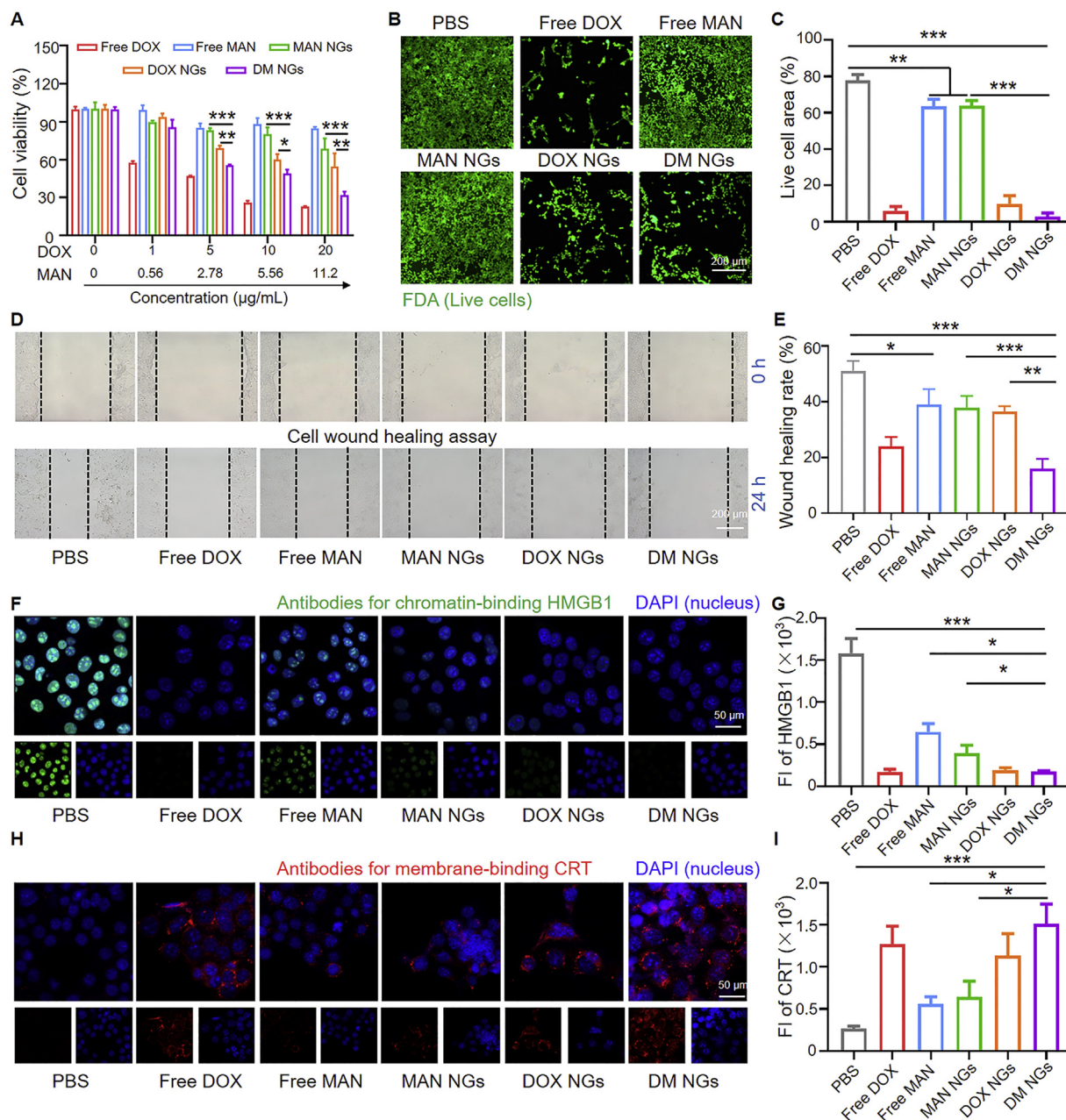


**Figure 2** Cytotoxicity and ICD studies of DM NGs *in vitro*. (A) Cytotoxicity of Free DOX, free MAN, MAN NGs, DOX NGs and DM NGs in 4T1 cells for 24 h. (B) Fluorescence images of 4T1 cells after treatments and FDA staining. (C) Area occupied by cells during live staining. (D) and (E) Scratch-wound healing assay. CLSM examinations of HMGB1 (F) and CRT (H) release. Fluorescence intensity of HMGB1 (G) and CRT (I) expressed. Data are presented as mean  $\pm$  SD ( $n = 3$ ). \* $P < 0.05$ ; \*\* $P < 0.01$ ; \*\*\* $P < 0.001$ .

delayed the growth of 4T1 cells, suggesting the moderate inhibitory effects. It was obvious that the free DOX, DOX NGs and DM NGs groups showed the less area with green fluorescence, indicating that nearly all the cells died. Finally, the cell migration ability of different NGs were examined by wound healing assay (Fig. 2D and E). At 24 h, the wound almost healed completely in control group, while the wound was hardly healed in the DM NGs. These results suggested that the DM NGs made an excellent inhibitory effect on cancer cell proliferation, enabling its a potential nanoagent for effective cancer treatment *in vivo*.

### 3.3. ICD induction of DM NGs *in vitro*

Recent studies have found that ICD could be induced with the treatment of DOX, which was benefit for anti-tumor immune response<sup>25,26</sup>. The ICD was accompanied by the exposure of CRT on cell membrane and the release of ATP and HMGB1. Various treatments induced translocation of the HMGB1 from nucleus to extracellular matrix, which were examined by immunofluorescence analysis. HMGB1 was a danger signal which activated a series of the related signaling pathways to promote tumorigenesis and proliferation<sup>27–30</sup>. As shown in Fig. 2F, the green fluorescence of all

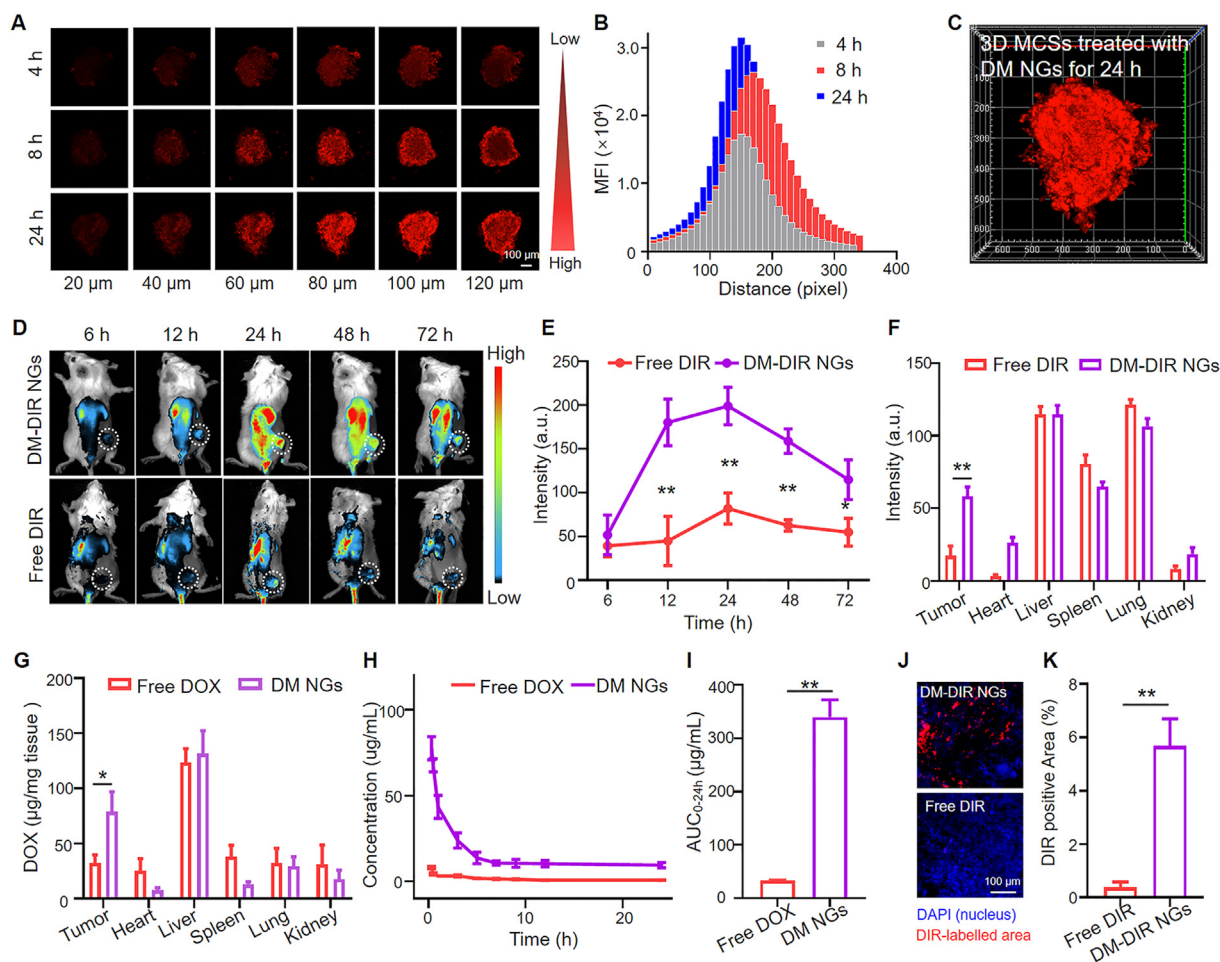


**Figure 3** Biodistribution and pharmacokinetics of DM NGs. (A) Penetration of DM NGs in 4T1 MCSs for 4, 8, and 24 h, respectively. (B) The mean fluorescence intensity of DOX in each layer in the MCSs. (C) *In vitro* tumor permeability of MCSs treated with DM NGs for 24 h. (D) Fluorescence imaging, and (E) Semi-quantitative fluorescence intensity of DM NGs distribution in 4T1 tumor-bearing mice *in vivo*. (F) The semi-quantitative fluorescence intensity of the tumor and major organs (heart, liver, spleen, lung, kidney) examined 72 h post-injection. (G) Quantification of DM NGs in tumor and major organs by fluorescence spectrophotometer. (H) Plasma concentration-time profiles and (I) the  $AUC_{0-24h}$  of DOX in SD rat post i.v. injection of DM NGs or Free DOX. (J) CLSM images and (K) quantification of DIR fluorescence distribution in tumor. Data are presented as mean  $\pm$  SD ( $n = 3$ ). \* $P < 0.05$ ; \*\* $P < 0.01$ ; \*\*\* $P < 0.001$ .

HMGB1 was located in the nucleus of control. The HMGB1 release was moderate after the treatment of free mannose and MAN NGs, while it was more significant in DM NGs and free DOX-treated groups. The mean intranuclear fluorescence intensity of HMGB1 in DM NGs-treated cells was much weaker than that of in control group (Fig. 2G). CRT was another potent marker for ICD, which served as a “eat me” signal of dying tumor cell and then induced phagocytosis of APCs. Thus CRT expression level was an important indicator of immune activation<sup>31–33</sup>. As shown in Fig. 2H, DOX was a potent chemoagent to induce robust CRT expression and ICD. The fluorescence of CRT was significantly increased on cell membrane of DM NGs group, compared with that of free mannose and DOX NGs groups (Fig. 2I). Detection of ATP secretion also found that DM NGs caused robust ATP release (Supporting Information Fig. S14). These results demonstrated that DM NGs could effectively induce the ICD, further enhance the antigen presentation and DCs maturation for modulating the tumor immunogenicity.

### 3.4. Pharmacokinetics and biodistribution

4T1 tumor MCSs were employed to assess the tissue penetration capability of DM NGs *in vitro* (Fig. 3A). After 4 h of incubation, the weak red fluorescence of the DM NGs could be observed in all the layer of MCSs. Upon incubation for 8 and 24 h, red fluorescence were gradually distributed throughout the whole spheroids and became stronger (Fig. 3B and C). Mean fluorescence intensity in 100  $\mu$ m of MCSs also proved the deep penetration capability of DM NGs in a time-dependent manner, which may be resulted from the nanoscale of NGs (Supporting Information Fig. S15).

The pharmacokinetics and biodistribution of the DM NGs were evaluated *in vivo*. The biodistribution was then analyzed on the mice bearing with 4T1 tumors. The DM NGs had no fluorescence on its own, and DIR was applied as the fluorescence dye to label the DM NGs (donated at DM-DIR NGs), with the free DIR as

control. DM-DIR NGs had an almost same size as DM NGs, indicating that the DIR had no influence on the formulation of DM NGs (Supporting Information Fig. S16). The distribution of the DM-DIR NGs in 4T1 tumor-bearing mice was observed. As showed in Fig. 3D and the semiquantitative fluorescence intensity analysis in Fig. 3E, the fluorescence intensity of tumor site became stronger with time, reached the strongest value after 24 h, indicating a strong enrichment effect of DM NGs at the tumor site. The fluorescence intensity was gradually weakened after 24 h, but strong fluorescence could be still seen at the tumor site, indicating that the drug had strong retention effect, resulted in the prolonged blood circulation time. On the contrary, the tumor homing ability of the free DIR group was poor, which may be due to the easy metabolite of free drugs through the kidney. After 72 h, the mice were sacrificed, then the major organs and solid tumor were dissected. As showed in Fig. 3F and Supporting Information Fig. S17, there was strong fluorescence in the tumor treated with DM-DIR NGs, but the free DIR was almost completely metabolized, which was proved by the tumor section. The red fluorescence of the DIR was clearly observed in DM-DIR NGs group, while almost no fluorescence was observed in free DIR group (Fig. 3J and K). The concentration of DOX in tumor and major organs were also measured by fluorescence spectrophotometer (Fig. 3G). The accumulation of DOX in tumor was significantly higher in DM NGs group, compared to that of free DOX group, while the DM NGs and free DOX in the major organs showed similar accumulation behavior. It might be related to the specific uptake of NGs by tumor cells. Collectively, the DM NGs had the characteristics of deep tumor penetration, long retention time and favorable fluorescence imaging, enabling its applications in fluorescence imaging-guided cancer therapy.

Given the excellent stability under physiological environment and good tumor retention, the pharmacokinetics of DM NGs was evaluated by determining the DOX concentration in the plasma. As showed in Fig. 3H, the elimination half-life ( $t_{1/2}$ ) of DM NGs and free DOX were evaluated with the pharmacokinetic model, which were calculated to be  $1.40 \pm 0.52$  and  $0.31 \pm 0.04$  h, respectively. It could be clearly seen that the DM NGs prolonged the blood circulation time of DOX, compared with free DOX. The area under the curves (AUCs) of DM NGs was 10-fold higher than free DOX, which proved the good retention ability of DM NGs. The effects of DM NGs could last for a long time, attributed to the nano-structure. Thus, the DM NGs exhibited both slower clearance rate and longer circulation time compared to free drugs (Fig. 3I).

### 3.5. *In vivo antitumor efficacy*

Based on the fact that DM NGs had outstanding inhibitory effects on tumor cells, its efficacy was further explored on 4T1-tumor-bearing mice. As shown in Fig. 4A, the intravenous injection was repeated on Days 0, 3, 6 and 9. During the 11 days of treatments, the average tumor volume in PBS-treated group was increased from  $\sim 152$  to  $\sim 1005$  mm<sup>3</sup>, while DM NGs treatment showed excellent tumor suppression rate, with a tumor weight loss of  $\sim 86\%$  (Fig. 4B and C). It might be induced by the treatment of mannose, which made the tumor cell more sensitive to DOX. The administration of free DOX made certain antitumor effects on the

mice, in which the body weight was significantly reduced due to the nonspecific distribution and fast clearance. The treatment of free mannose and MAN NGs also inhibited the growth of tumor. The tumor photos of different groups and tumor weight recorded at the end of treatments (11 days) further demonstrated the excellent synergistic therapeutic effects of DOX and mannose (Fig. 4D and Supporting Information Figs. S19 and S20). The body weight of mice in the free DOX group was significantly decreased, while it was not noticeable in mice of all other groups (Supporting Information Fig. S18). Furthermore, the survival time of different groups was also evaluated. As shown in Fig. 4E, the DM NGs can effectively prolong the survival time of mice, which may be resulted from that DM NGs can ameliorate the immune microenvironment. For H&E staining, the tumor tissues in control group appeared to be more hypercellular, while the DM NGs-treated group showed significant tumor cell necrosis. Meanwhile, the Ki67 staining demonstrated less cell proliferation in the DM NGs. Additionally, TUNEL-staining showed that DM NGs likely induced more tumor cell apoptosis/necrosis (Fig. 4F). The quantitative Ki67 positive area and corresponding tumor cell apoptosis index in different groups were shown in Fig. 4G and H, respectively.

### 3.6. *In vivo immune response of DM NGs*

Based on the significant therapeutic performance and prolonged survival time in mice, we speculated whether the synergetic antitumor effects of mannose and DOX were achieved by remodeling TME and immune system. Improving the infiltration of T cells in TME was essential for cancer immunotherapy. It was reported that mannose could relieve the immunosuppressive state<sup>58</sup>. Therefore, tumor and DLN tissues were collected after different treatments for FCM analysis. Firstly, the number of T cells was explored by FCM. As shown in Supporting Information Fig. S21, the CD3<sup>+</sup> cell population was gated from CD45<sup>+</sup> cell population. Then CD8<sup>+</sup> cell subpopulation was further gated. Further, the expression of TIM-3 and PD-1 in CD8<sup>+</sup> cells was quantified. The total CD8<sup>+</sup> cell population was not changed in each group as indicated by FCM and IHC (Supporting Information Figs. S22 and S23). Improved expression of PD-1 and TIM-3 in T cells promoted T cell exhaustion<sup>59,60</sup>. The high expression of PD-1 and TIM-3 indicated the exhaustion of T cells, and the reduced T cell exhaustion meant the improvement of the ITM. Both the PD-1<sup>+</sup> CD8<sup>+</sup> cell population and PD-1<sup>+</sup> TIM-3<sup>+</sup> CD8<sup>+</sup> cell population were detected from single-cell suspension obtained from tumor and DLN. Interestingly, DOX NGs and DM NGs treatment significantly reduced the rate of PD-1<sup>+</sup> TIM-3<sup>+</sup> CD8<sup>+</sup> T cells in TME (Fig. 5A and B), compared with that of other group. It may be due to the improved balance between efficacy and toxicity of the nanomedicine (Fig. 5C–E). Above data suggested that TME response of DM NGs could reduce the exhaustion of CD8<sup>+</sup> T cell, thus regulating the TME and improving the antitumor effects.

Furthermore, we explored whether DM NGs might react to T cells, thus amplifying the immunoactivity of T cells in TME. As reported, cytotoxic T cells functioned as a killer by secreting enzyme Granzyme B. The IHC of Granzyme B confirmed the increased immunoreactivity in free DOX, DOX NGs and DM NGs

groups (Fig. 5F and G). Together, these results suggested that DM NGs treatment could reinvigorate effector T cells. ICD, one of the most efficient ways for cancer therapy, has been reported to play a vital role in antitumor immune responses and promote immune recognition of chemotherapy. *In vitro* experiment showed that DM NGs treatment could induce robust ICD in 4T1 cells (Fig. 2F and H). ICD activated the antitumor response by promoting the maturation of DCs. Thus, the potent markers of CD80 and CD86 population could be applied to characterize the maturation of DCs.

As the result, the population of CD80<sup>+</sup>CD86<sup>+</sup> DCs in DLN was significantly increased in the DM NGs-treated group in comparison to PBS group (Fig. 6A and B, Supporting Information Figs. S24 and S25). As shown in Fig. 6C and D, compared with control group, the DM NGs-treated group showed more yellow fluorescence, indicating improved antitumor response. As APCs, tumor-associated antigens (TAAs) can be transported into tumor lymph nodes by CD103 cells, thus inducing robust CD8<sup>+</sup> T cells to produce immune response<sup>61</sup>. Furthermore, the DM NGs significantly increased the CD103 expression of DCs compared

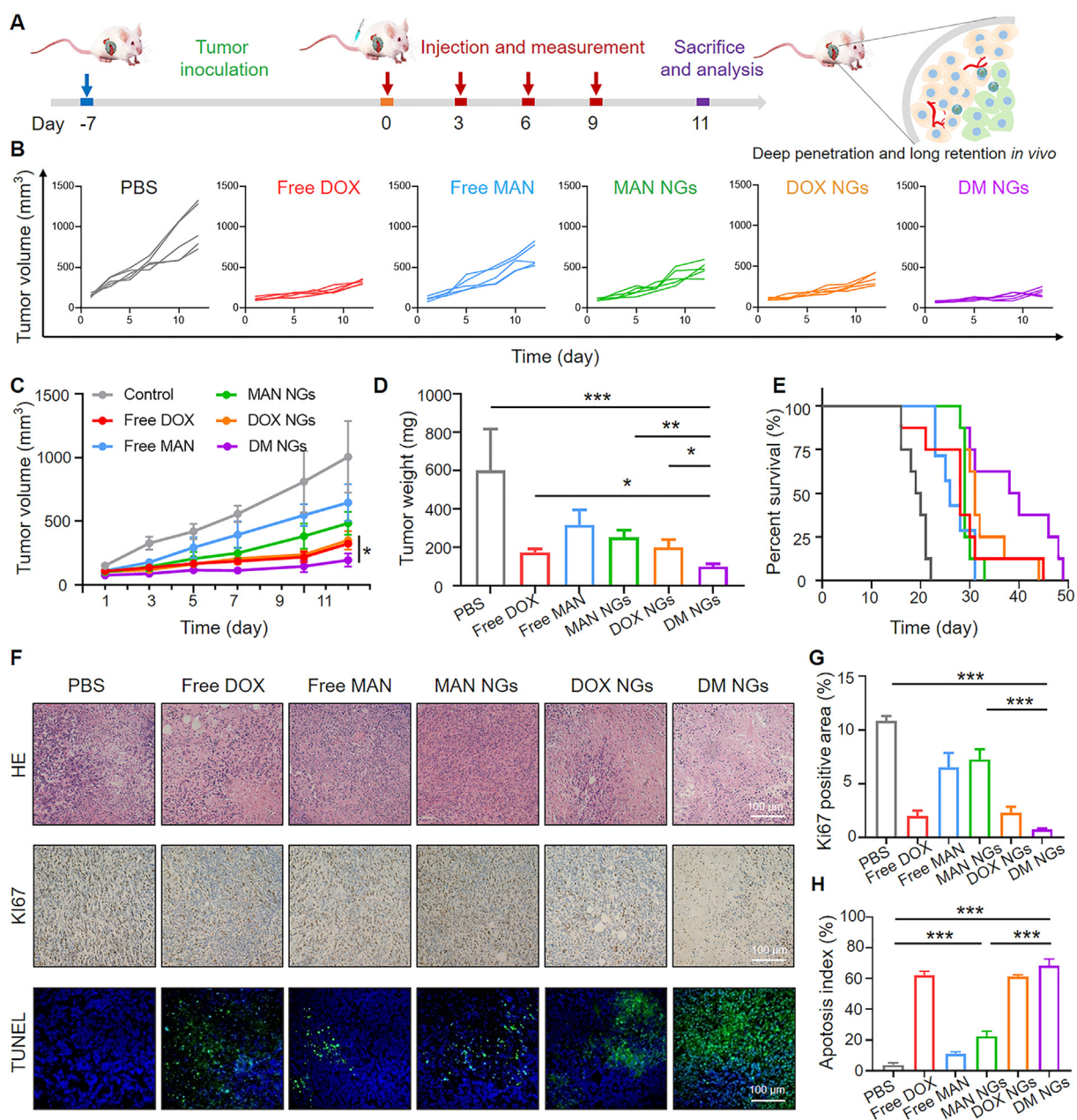


**Figure 4** Antitumor efficacy of DM NGs on balb/c mice bearing 4T1 tumor. (A) The therapeutic schedule, deep penetration and long residence of DM NGs *in vivo* study. (B) Individual tumor growth curves and (C) average tumor growth curves after different treatments. (D) Average tumor weight after 11 days of treatment in various groups. (E) Survival curves of model mice ( $n = 8$ ). (F) H&E (upper panel), Ki67 (middle panel) and TUNEL staining (lower panel) of tumor tissues after various treatments for 11 days. (G) Quantification of Ki67 proliferative cells ratio in panel. (H) The corresponding tumor apoptosis index. Data are presented as mean  $\pm$  SD ( $n = 5$ ). \* $P < 0.05$ ; \*\* $P < 0.01$ ; \*\*\* $P < 0.001$ .

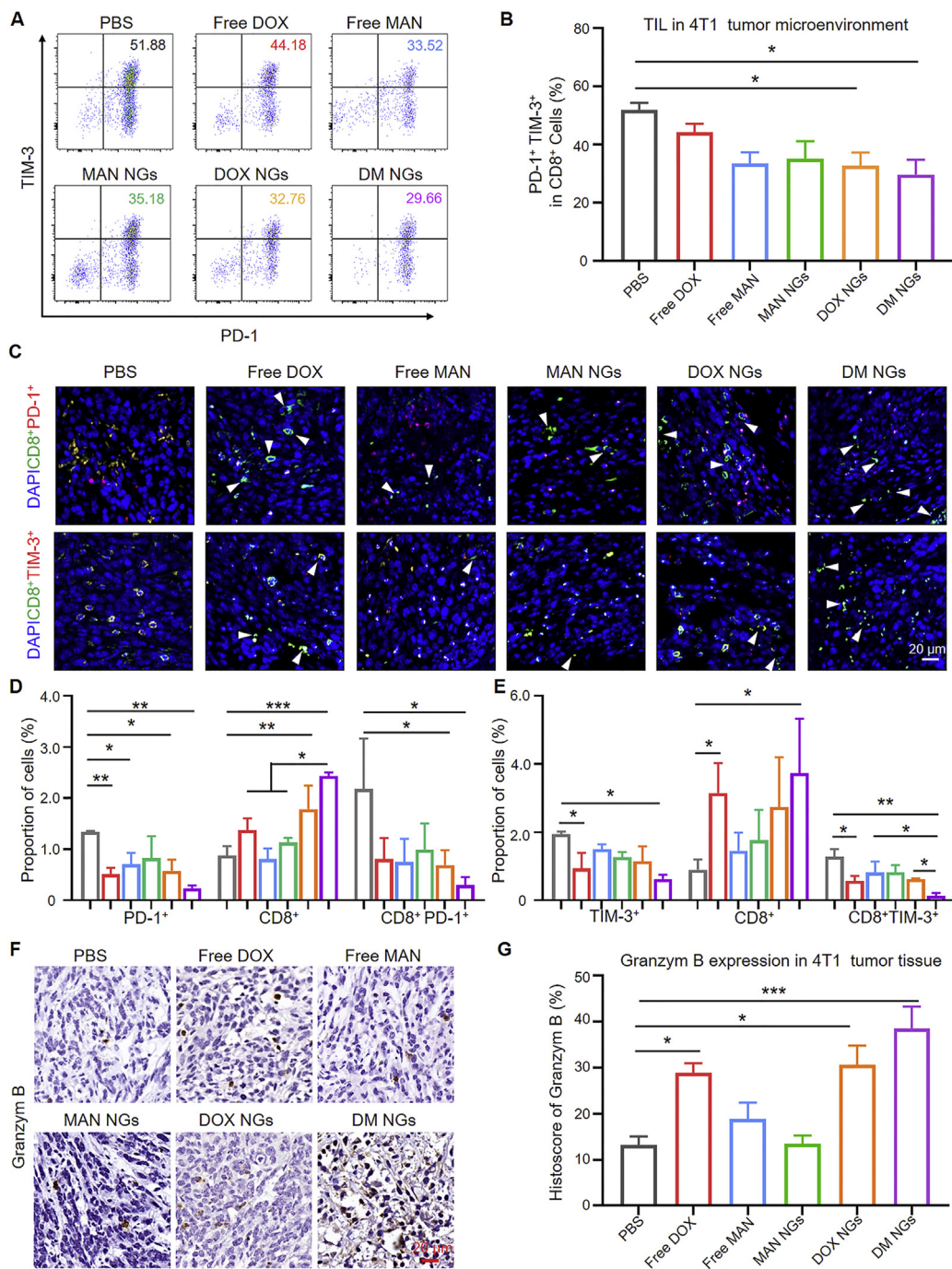


**Figure 5** Immune checkpoint PD-1 and TIM-3 expression on CD4<sup>+</sup> and CD8<sup>+</sup> T-cell subsets. (A) Representative flow cytometry data for PD-1<sup>+</sup>TIM-3<sup>+</sup> CD8<sup>+</sup> T cells in tumor. (B) Quantification of PD-1<sup>+</sup>TIM-3<sup>+</sup> in CD8<sup>+</sup> cells. (C) Phenotype, distribution, and localization of TIM-3<sup>+</sup> CD8<sup>+</sup> T cells in 4T1 tumor tissue. The white arrow indicate activated T cell. (D) and (E) Quantification of two color immunofluorescence staining. Expression (F) and quantification (G) of Granzym B in tumor tissue of different groups. Data are presented as mean  $\pm$  SD ( $n = 5$ ). \* $P < 0.05$ ; \*\* $P < 0.01$ ; \*\*\* $P < 0.001$ .

with other groups, indicating enhanced TAAs presenting and improved tumor immunity (Fig. 6E–F and Supporting Information Figs. S26 and S27). Then we studied the tumor-associated macrophages (TAM) change in TME, and the DM NGs reduced the number of TAM from 32.7% to 21.7% compared with control group (Supporting Information Figs. S28 and S29). All these results suggest that DM NGs can induce robust T cell response,

which was conducive to awakening the immune system to fight against tumors.

To further prove that ICD may cause the reinvigoration of T cell and the maturation of DCs, ICD was characterized in 4T1 tumor tissues (Fig. 7A). The induction of ICD was further confirmed by predominant nuclear expression of HMGB1 in free DOX group and DM NGs group (Fig. 7B and C). The DM NGs

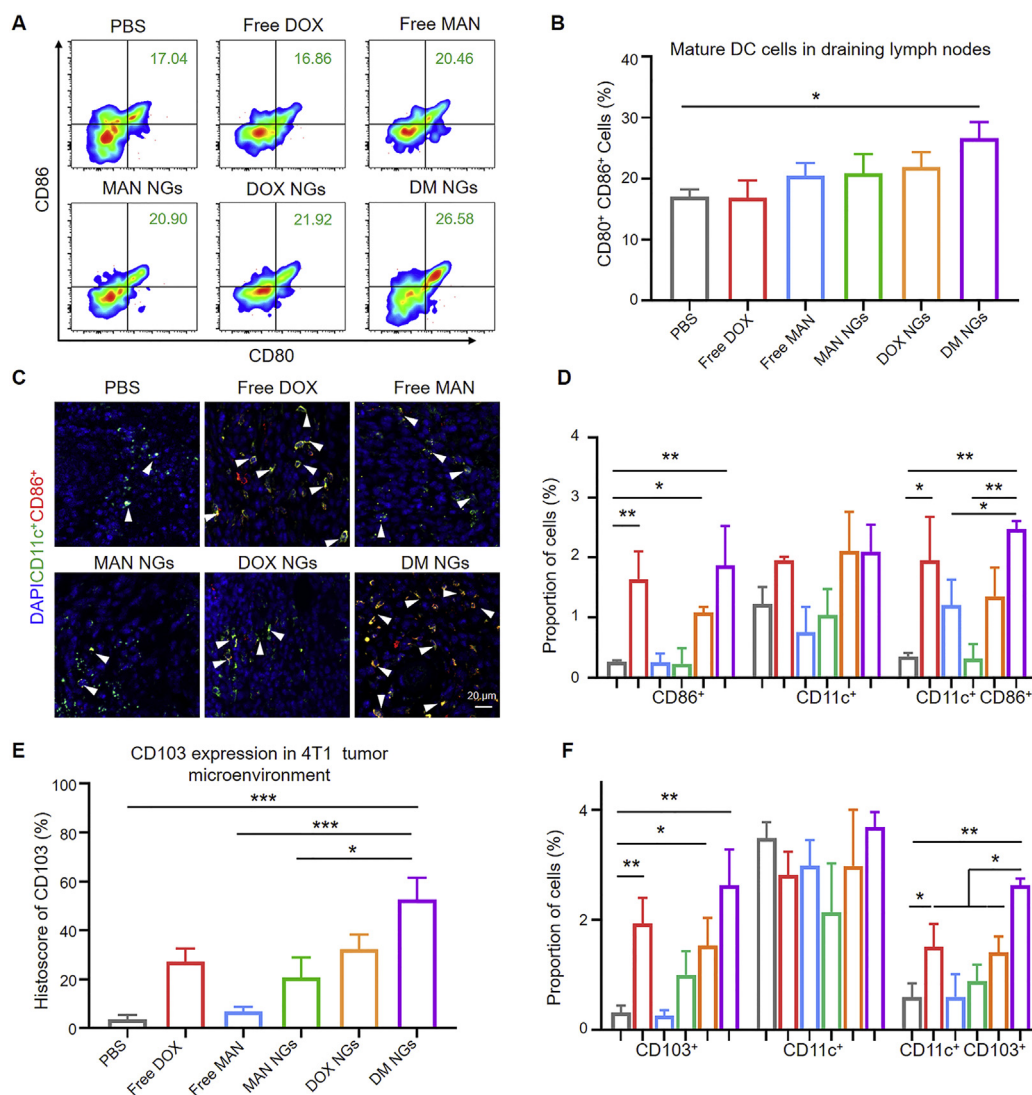


**Figure 6** DCs maturation of DM NGs. (A) Representative flow cytometry images (B) and quantification results for mature DCs in DLN. (C) Phenotype, distribution, and localization of CD11c<sup>+</sup>CD86<sup>+</sup> cells in 4T1 tumor tissue. The white arrow indicate activated T cell. (D) Quantification of two color immunofluorescence staining by Image J software. (E) Quantification of CD103 cells in tumor tissue of different groups. (F) Quantification of two color immunofluorescence staining. Data are presented as mean  $\pm$  SD ( $n = 5$ ). \* $P < 0.05$ ; \*\* $P < 0.01$ ; \*\*\* $P < 0.001$ .

group significantly reduced cytoplasm expression as compared with free DOX, MAN NGs and DOX NGs groups. As indicated in Fig. 7D and E, CRT immunofluorescence was significantly increased on membrane of dying 4T1 cells in DM NGs groups, compared with MAN NGs and DOX NGs groups according to the corresponding quantification results of mean fluorescence intensity (MFI) (Fig. 7E). It indicated that the combination of DOX and mannose in DM NGs might synergistically induce ICD as well as remodeling TME. The ICD-induced DM NGs produced better immunotherapeutic effects than free DOX, and the key reason was that the DM NGs could be selectively accumulated at the tumor site, leading to a reduction in systemic immunosuppression. These results collectively confirmed that DM NGs group predominantly induced ICD, promoted DCs maturation and rein-

vigorated T cells, thus making anti-tumor effects and ameliorating the TME.

Finally, the *in vitro* and *in vivo* toxicology were investigated systematically, as well as the potential side effects. Firstly, the compatibility of the DM NGs was verified by measuring the hemolysis rate. The hemolysis rate was still less than 5% even when the concentration of the DOX in the DM NGs reached 500  $\mu\text{g/mL}$ , indicating the excellent blood compatibility and micellar stability of DM NGs, which was conducive to prolonging the blood circulation (Supporting Information Fig. S30). After the healthy mice received intravenous injection of different drugs, the weight change of mice was negligible. The blood routine and H&E staining also proved the excellent biosafety (Supporting Information Figs. S31 and S33). The safety of our NGs was evaluated

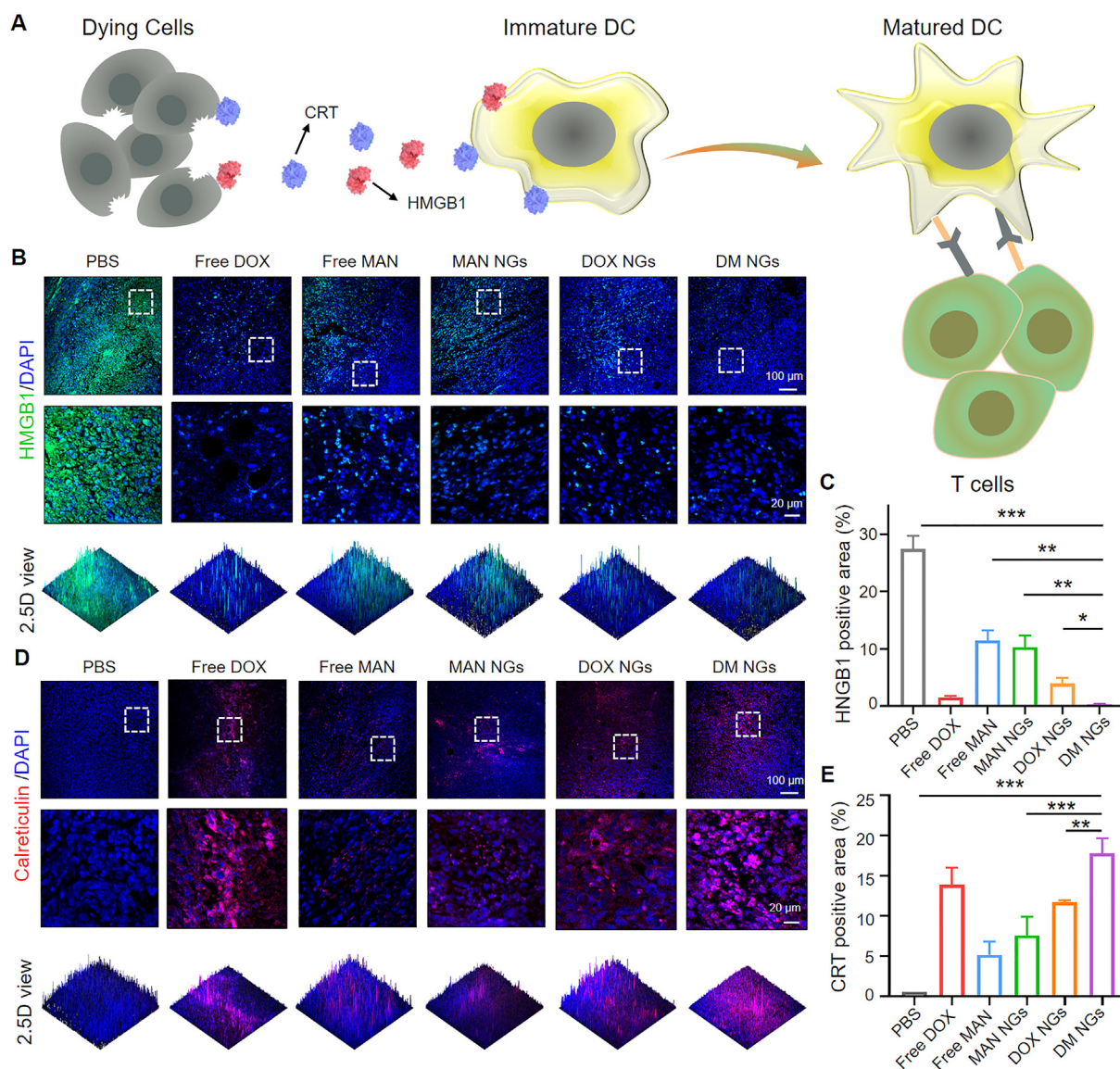


**Figure 7** ICD of DM NGs *in vivo*. (A) Schematic illustration of DM NGs-mediated activation mechanism of DCs maturation. (B) Immunofluorescence staining of HMGB1 release in 4T1 tumors and (C) corresponding quantifications. (D) Immunofluorescence staining of CRT exposure in 4T1 tumors and (E) corresponding quantifications. Data are presented as mean  $\pm$  SD ( $n = 5$ ). \* $P < 0.05$ ; \*\* $P < 0.01$ ; \*\*\* $P < 0.001$ .

on 4T1 tumor-bearing nude mice after different treatments. As shown in Supporting Information Fig. S34, treatment of free DOX exhibited obvious abnormality of heart, indicated by the swelling myocardial fibers and cardiomyocyte vacuolation. In addition, no obvious histopathological abnormality was found in the DM NGs-treated group. Furthermore, the blood levels of ALT, AST, CRE, urea, LDH and ALKP were not significantly varied with those of in control group, further confirming the safe application of nanogel in chemo-immunotherapy.

#### 4. Conclusions

In summary, we have reported a universal DOX-based bio-responsive NGs to facilitate the combination of chemotherapy and immunotherapy. DM NGs displayed prolonged blood circulation and enhanced tumor accumulation compared with free DOX. DM NGs could induce robust ICD, enhance the migration of CRT to

the cell membrane, stimulate DCs phagocytosis, release HMGB1, and promote specific T cell antitumor immunity. Meanwhile, mannose released by DM NGs could impair the metabolism of glucose in glycolysis and the tricarboxylic acid cycle, thus regulating tumor metabolism and finally leading to the apoptosis of cancer cells. Consequently, DOX-based NGs could be easily extended to other small-molecule drugs besides of mannose reported in this study. Taken together, this bio-responsive DOX-based NGs strategy can systematically regulate the TME and improve ITM, providing bright application prospects in chemo-therapy and immunotherapy of solid tumors.

#### Acknowledgements

This work was financially supported by National Natural Science Foundation of China (51703187, 81874131, and 81672668), the Chongqing Talent Plan for Young TopNotch Talents (CQYC202005029, China),

Major State Basic Research Development Program of China (2017YFA0205201 and 2018YFA0107301), National Key Research and Development Program (2017YFSF090107, China), the Hubei Province Natural Science Funds for Distinguished Young Scholar 2017CFA062.

### Author contributions

Zhigang Xu, Zhijun Sun and Gang Liu designed the research. Xianbin Ma and Shaochen Yang carried out the experiments and performed data analysis. Tian Zhang, Shuo Wang, Qichao Yang, Yao Xiao and Xiaoxiao Shi participated part of the experiments. Peng Xue and Yuejun Kang provided experimental drugs and quality control. Xianbin Ma and Shaochen Yang wrote the manuscript. Zhigang Xu revised the manuscript. All of the authors have read and approved the final manuscript.

### Conflicts of interest

The authors have no conflicts of interest to declare.

### Appendix A. Supporting information

Supporting data to this article can be found online at <https://doi.org/10.1016/j.apsb.2021.05.016>.

### References

- Bray F, Ferlay J, Soerjomataram I, Siegel RL, Torre LA, Jemal A. Global cancer statistics 2018: GLOBOCAN estimates of incidence and mortality worldwide for 36 cancers in 185 countries. *CA Canc J Clin* 2018;**68**:394–424.
- Kalbasi A, Ribas A. Tumour-intrinsic resistance to immune checkpoint blockade. *Nat Rev Immunol* 2020;**20**:25–39.
- Keenan TE, Burke KP, Van Allen EM. Genomic correlates of response to immune checkpoint blockade. *Nat Med* 2019;**25**:389–402.
- Wolchok JD, Chiarion-Sileni V, Gonzalez R, Rutkowski P, Grob JJ, Cowey CL, et al. Overall survival with combined nivolumab and ipilimumab in advanced melanoma. *N Engl J Med* 2017;**377**:1345–56.
- Turley SJ, Cremasco V, Astarita JL. Immunological hallmarks of stromal cells in the tumour microenvironment. *Nat Rev Immunol* 2015;**15**:669–82.
- Patel SA, Minn AJ. Combination cancer therapy with immune checkpoint blockade: mechanisms and strategies. *Immunity* 2018;**48**:417–33.
- Fan Q, Chen Z, Wang C, Liu Z. Toward biomaterials for enhancing immune checkpoint blockade therapy. *Adv Funct Mater* 2018;**28**:1802540.
- Chen Y, Song W, Shen L, Qiu N, Hu M, Liu Y, et al. Vasodilator hydralazine promotes nanoparticle penetration in advanced desmoplastic tumors. *ACS Nano* 2019;**13**:1751–63.
- Broz P, Monack DM. Newly described pattern recognition receptors team up against intracellular pathogens. *Nat Rev Immunol* 2013;**13**:551–65.
- Muraoka D, Seo N, Hayashi T, Tahara Y, Fujii K, Tawara I, et al. Antigen delivery targeted to tumor-associated macrophages overcomes tumor immune resistance. *J Clin Invest* 2019;**129**:1278–94.
- Yu GT, Rao L, Wu H, Yang LL, Bu LL, Deng WW, et al. Myeloid-derived suppressor cell membrane-coated magnetic nanoparticles for cancer theranostics by inducing macrophage polarization and synergizing immunogenic cell death. *Adv Funct Mater* 2018;**28**:1801389.
- Schumacher TN, Schreiber RD. Neoantigens in cancer immunotherapy. *Science* 2015;**348**:69.
- Galluzzi L, Buqué A, Kepp O, Zitvogel L, Kroemer G. Immunogenic cell death in cancer and infectious disease. *Nat Rev Immunol* 2017;**17**:97–111.
- Kroemer G, Galluzzi L, Kepp O, Zitvogel L. Immunogenic cell death in cancer therapy. *Annu Rev Immunol* 2013;**31**:51–72.
- Krysko DV, Garg AD, Kaczmarek A, Krysko O, Agostinis P, Vandenabeele P. Immunogenic cell death and DAMPs in cancer therapy. *Nat Rev Cancer* 2012;**12**:860–75.
- Valpione S, Galvani E, Tweedy J, Mundra PA, Banyard A, Middlehurst P, et al. Immune awakening revealed by peripheral T cell dynamics after one cycle of immunotherapy. *Nat Cancer* 2020;**1**:210–21.
- Chapman NM, Boothby MR, Chi H. Metabolic coordination of T cell quiescence and activation. *Nat Rev Immunol* 2020;**20**:55–70.
- Vacchelli E, Ma Y, Baracco EE, Sistigu A, Enot DP, Pietrocola F, et al. Chemotherapy-induced antitumor immunity requires formyl peptide receptor 1. *Science* 2015;**350**:972.
- Feng B, Niu Z, Hou B, Zhou L, Li Y, Yu H. Enhancing triple negative breast cancer immunotherapy by ICG-templated self-assembly of paclitaxel nanoparticles. *Adv Funct Mater* 2020;**30**:1906605.
- Yu Z, Guo J, Hu M, Gao Y, Huang L. Icaritin exacerbates mitophagy and synergizes with doxorubicin to induce immunogenic cell death in hepatocellular carcinoma. *ACS Nano* 2020;**14**:4816–28.
- Chao Y, Liang C, Tao H, Du Y, Wu D, Dong Z, et al. Localized cocktail chemoimmunotherapy after *in situ* gelation to trigger robust systemic antitumor immune responses. *Sci Adv* 2020;**6**:eaaz4204.
- Kuai R, Yuan W, Son S, Nam J, Xu Y, Fan Y, et al. Elimination of established tumors with nanodisc-based combination chemoimmunotherapy. *Sci Adv* 2018;**4**:eaao1736.
- Su B, Cengizeroglu A, Farkasova K, Viola JR, Anton M, Ellwart JW, et al. Systemic TNF $\alpha$  gene therapy synergizes with liposomal doxorubicin in the treatment of metastatic cancer. *Mol Ther* 2013;**21**:300–8.
- Li S, Wang Q, Shen Y, Hassan M, Shen J, Jiang W, et al. Pseudo-neutrophil cytokine sponges disrupt myeloid expansion and tumor trafficking to improve cancer immunotherapy. *Nano Lett* 2020;**20**:242–51.
- Obeid M, Tesniere A, Ghiringhelli F, Fimia GM, Apetoh L, Perfettini JL, et al. Calreticulin exposure dictates the immunogenicity of cancer cell death. *Nat Med* 2007;**13**:54–61.
- Lu J, Liu X, Liao YP, Salazar F, Sun B, Jiang W, et al. Nano-enabled pancreas cancer immunotherapy using immunogenic cell death and reversing immunosuppression. *Nat Commun* 2017;**8**:1811.
- Yu L, Wang Z, Mo Z, Zou B, Yang Y, Sun R, et al. Synergetic delivery of triptolide and Ce6 with light-activatable liposomes for efficient hepatocellular carcinoma therapy. *Acta Pharm Sin B* 2021;**11**:2004–15.
- Shi J, Kantoff PW, Wooster R, Farokhzad OC. Cancer nanomedicine: progress, challenges and opportunities. *Nat Rev Canc* 2017;**17**:20–37.
- Blanco E, Shen H, Ferrari M. Principles of nanoparticle design for overcoming biological barriers to drug delivery. *Nat Biotechnol* 2015;**33**:941–51.
- van der Meel R, Sulheim E, Shi Y, Kiessling F, Mulder WJM, Lammers T. Smart cancer nanomedicine. *Nat Nanotechnol* 2019;**14**:1007–17.
- Dai Y, Xu C, Sun X, Chen X. Nanoparticle design strategies for enhanced anticancer therapy by exploiting the tumour microenvironment. *Chem Soc Rev* 2017;**46**:3830–52.
- Peer D, Karp JM, Hong S, Farokhzad OC, Margalit R, Langer R. Nanocarriers as an emerging platform for cancer therapy. *Nat Nanotechnol* 2007;**2**:751–60.
- Zhang P, Wang J, Chen H, Zhao L, Chen B, Chu C, et al. Tumor microenvironment-responsive ultrasmall nanodrug generators with enhanced tumor delivery and penetration. *J Am Chem Soc* 2018;**140**:14980–9.
- Shi X, Zhang Y, Tian Y, Xu S, Ren E, Bai S, et al. Multi-responsive nanotheranostic-based bottlebrush-like unimolecules self-assembled

- nano-riceball for synergistic sono-chemotherapy. *Small Methods* 2021; **5**:2000416.
35. Kabanov AV, Vinogradov SV. Nanogels as pharmaceutical carriers: finite networks of infinite capabilities. *Angew Chem Int Ed* 2009; **48**: 5418–29.
  36. Song Q, Yin Y, Shang L, Wu T, Zhang D, Kong M, et al. Tumor micro-environment responsive nanogel for the combinatorial antitumor effect of chemotherapy and immunotherapy. *Nano Lett* 2017; **17**:6366–75.
  37. Zuo L, Ding J, Li C, Lin F, Chen PR, Wang P, et al. Coordinating bioorthogonal reactions with two tumor-microenvironment-responsive nanovehicles for spatiotemporally controlled prodrug activation. *Chem Sci* 2020; **11**:2155–60.
  38. Willems Peter HGM, Rossignol R, Dieteren Cindy EJ, Murphy Michael P, Koopman Werner JH. Redox homeostasis and mitochondrial dynamics. *Cell Metab* 2015; **22**:207–18.
  39. Ma X, Zhang T, Qiu W, Liang M, Gao Y, Xue P, et al. Bioresponsive prodrug nanogel-based polycondensate strategy deepens tumor penetration and potentiates oxidative stress. *Chem Eng J* 2020:127657.
  40. Ma S, Song W, Xu Y, Si X, Lv S, Zhang Y, et al. Rationally designed polymer conjugate for tumor-specific amplification of oxidative stress and boosting antitumor immunity. *Nano Lett* 2020; **20**:2514–21.
  41. Lin H, Li S, Wang J, Chu C, Zhang Y, Pang X, et al. A single-step multi-level supramolecular system for cancer sonotheranostics. *Nanoscale Horiz* 2019; **4**:190–5.
  42. Zhou Q, Shao S, Wang J, Xu C, Xiang J, Piao Y, et al. Enzyme-activatable polymer–drug conjugate augments tumour penetration and treatment efficacy. *Nat Nanotechnol* 2019; **14**:799–809.
  43. Bai S, Jia D, Ma X, Liang M, Xue P, Kang Y, et al. Cylindrical polymer brushes-anisotropic unimolecular micelle drug delivery system for enhancing the effectiveness of chemotherapy. *Bioactive Mater* 2021; **6**:2894–904.
  44. Jiang J, Shen N, Ci T, Tang Z, Gu Z, Li G, et al. Combretastatin A4 nanodrug-induced MMP9 amplification boosts tumor-selective release of doxorubicin prodrug. *Adv Mater* 2019; **31**:1904278.
  45. Bai S, Yang LL, Wang Y, Zhang T, Fu L, Yang S, et al. Prodrug-based versatile nanomedicine for enhancing cancer immunotherapy by increasing immunogenic cell death. *Small* 2020; **16**:2000214.
  46. Zou J, Zhu J, Yang Z, Li L, Fan W, He L, et al. A phototheranostic strategy to continuously deliver singlet oxygen in the dark and hypoxic tumor microenvironment. *Angew Chem Int Ed* 2020; **59**:8833–8.
  47. Afonso J, Santos LL, Longatto-Filho A, Baltazar F. Competitive glucose metabolism as a target to boost bladder cancer immunotherapy. *Nat Rev Urol* 2020; **17**:77–106.
  48. Warburg O. On the origin of cancer cells. *Science* 1956; **123**:309.
  49. Meng Z, Zhou X, Xu J, Han X, Dong Z, Wang H, et al. Light-triggered *in situ* gelation to enable robust photodynamic-immunotherapy by repeated stimulations. *Adv Mater* 2019; **31**:1900927.
  50. Vander Heiden MG, Cantley LC, Thompson CB. Understanding the Warburg effect: the metabolic requirements of cell proliferation. *Science* 2009; **324**:1029.
  51. Yang B, Chen Y, Shi J. Tumor-specific chemotherapy by nanomedicine-enabled differential stress sensitization. *Angew Chem Int Ed* 2020; **59**:9693–701.
  52. Zhang D, Chia C, Jiao X, Jin W, Kasagi S, Wu R, et al. D-Mannose induces regulatory T cells and suppresses immunopathology. *Nat Med* 2017; **23**:1036–45.
  53. Pavlova Natalya N, Thompson Craig B. The emerging hallmarks of cancer metabolism. *Cell Metab* 2016; **23**:27–47.
  54. Gonzalez PS, O'Prey J, Cardaci S, Barthelet VJA, Sakamaki JL, Beaumatin F, et al. Mannose impairs tumour growth and enhances chemotherapy. *Nature* 2018; **563**:719–23.
  55. Coniot J, Scomparin A, Peres C, Yeini E, Pozzi S, Matos AI, et al. Immunization with mannose-derivatized nanovaccines and inhibition of the immune-suppressing microenvironment sensitizes melanoma to immune checkpoint modulators. *Nat Nanotechnol* 2019; **14**:891–901.
  56. Zhong X, Wang X, Cheng L, Tang Ya, Zhan G, Gong F, et al. GSH-depleted PtCu<sub>3</sub> nanocages for chemodynamic-enhanced sonodynamic cancer therapy. *Adv Funct Mater* 2020; **30**: 1907954.
  57. Wang S, Li F, Qiao R, Hu X, Liao H, Chen L, et al. Arginine-rich manganese silicate nanobubbles as a ferroptosis-inducing agent for tumor-targeted theranostics. *ACS Nano* 2018; **12**:12380–92.
  58. Chen B, Gao A, Tu B, Wang Y, Yu X, Wang Y, et al. Metabolic modulation *via* mTOR pathway and anti-angiogenesis remodels tumor microenvironment using PD-L1-targeting codelivery. *Biomaterials* 2020; **255**:120187.
  59. Ribas A, Wolchok JD. Cancer immunotherapy using checkpoint blockade. *Science* 2018; **359**:1350.
  60. Tang R, Rangachari M, Kuchroo VK. Tim-3: a co-receptor with diverse roles in T cell exhaustion and tolerance. *Semin Immunol* 2019; **42**:101302.
  61. Roberts EW, Broz ML, Binnewies M, Headley MB, Nelson AE, Wolf DM, et al. Critical role for CD103<sup>+</sup>/CD141<sup>+</sup> dendritic cells bearing CCR7 for tumor antigen trafficking and priming of T cell immunity in melanoma. *Cancer Cell* 2016; **30**:324–36.